Research Article Vol. 4, No. 5 / 15 May 2021 / OSA Continuum 1461

Analysis of signal-to-noise ratio of angle of polarization and degree of polarization

YINGKAI CHEN,[1] ZHONGMIN ZHU,[1] ZUODONG LIANG,[1] LEANNE E. IANNUCCI,[2] SPENCER P. LAKE,[2,3,4] AND VIKTOR GRUEV[1,*]

[1] *University of Illinois at Urbana-Champaign, Department of Electrical and Computer Engineering, Urbana, Illinois 61801, USA*
[2] *Washington University in St. Louis, Department of Biomedical Engineering, St. Louis, Missouri 63130, USA*
[3] *Washington University in St. Louis, Department of Mechanical Engineering & Materials Science, St. Louis, Missouri 63130, USA*
[4] *Washington University in St. Louis, Department of Orthopedic Surgery, St. Louis, Missouri 63130, USA*
[*] *vgruev@illinois.edu*

Abstract: Recent advancements in nanofabrication technology has led to commercialization of single-chip polarization and color-polarization imaging sensors in the visible spectrum. Novel applications have arisen with the emergence of these sensors leading to questions about noise in the reconstructed polarization images. In this paper, we provide theoretical analysis for the input and output referred noise for the angle and degree of linear polarization information. We validated our theoretical model with experimental data collected from a division of focal plane polarization sensor. Our data indicates that the noise in the angle of polarization images depends on both incident light intensity and degree of linear polarization and is independent of the incident angle of polarization. However, noise in degree of linear polarization images depends on all three parameters: incident light intensity, angle and degree of linear polarization. This theoretical model can help guide the development of imaging setups to record optimal polarization information.

© 2021 Optical Society of America under the terms of the OSA Open Access Publishing Agreement

1. Introduction

Advancements in nanofabrication technology over the last decade has led to the development and commercialization of both single-chip polarization and color-polarization imaging sensors in the visible spectrum [1]. These novel polarization sensors, often described as division of focal plane [2–8] or bio-inspired sensors [9–12], monolithically combine pixelated polarization filters with an array of CCD or CMOS imaging elements. Several technological challenges had to be overcome to make this technology a viable commercial success. First, nanofabrication challenges associated with fabrication of pixelated polarization filters and integration with an array of imaging elements had to be addressed [8,13,14]. The size of the nanowires that comprise individual pixelated polarization filters must be at least 5 times smaller than the shortest wavelength of interest. For example, to capture polarization properties of a target in the blue spectrum (i.e., 400 nm wavelength), the width of the nanowires should be less than 80 nm. Although today's advanced CMOS technology can fabricate transistors and metallic lines with sizes of around 20 nm or less, these fabrication features are typically only available for digital circuits and not for analog circuits and imaging sensors. Imaging sensors are fabricated in larger feature technologies (90 nm or larger) with optimized photodiodes to achieve low noise (temporal and dark current) and high quantum efficiency sensors [15]. Hence, polarization filters had to be fabricated using specialized lithography processes not typically available for imaging technology. Second, combining color and polarization imaging on a single chip further introduced complexity and cost in the fabrication process. Color filters are realized using various polymers while polarization filters are fabricated

#422541 https://doi.org/10.1364/OSAC.422541
Journal © 2021 Received 24 Feb 2021; revised 5 Apr 2021; accepted 11 Apr 2021; published 26 Apr 2021

OSA CONTINUUM

using aluminum nanowires – two fabrication technologies that are incompatible. Monolithic integration of both types of filters required extensive research and development. An alternative approach is to use vertically stacked photodiodes with pixelated polarization filters to sense both color and polarization properties [10]. The fabrication complexity and cost in the latter case is shifted from the filters to the CMOS fabrication of the vertically stacked photodiodes.

The first single-chip polarization imaging sensor for the visible spectrum was achieved by integration of pixelated polarization filters with an array of CCD elements [3]. This concept was later extended to incorporate both color and polarization information by using vertically stacked photodiodes as a substrate [10,16]. Since 2018, Sony has made polarization imaging technology commercially available [1]. Over the last decade, many new applications have emerged which have taken advantage of the single chip architecture for polarization imaging, such as early cancer detection [17,18], underwater geolocalization [19], aerosol monitoring [20,21], discovery of new polarization-based behaviors in marine animals [22–24], computer vision applications [25–27] and microstructural analysis of collagenous tissues [28,29].

The emergence of new applications spearheaded by the development of single-chip polarization cameras has raised questions regarding signal-to-noise (SNR) ratio in polarization images, namely output metrics of angle of polarization (*AoP*) and degree of linear polarization (*DoLP*). Since many application-specific algorithms are based on *AoP* and *DoLP* images, the noise properties of these images are typically directly correlated to the confidence in the observed results: higher SNR in *AoP* and *DoLP* images means higher confidence in the observed polarization-based physical phenomena. For example, accurate identification and differentiation of cancerous tissue from healthy tissue based on light scattering recorded with *AoP* and *DoLP* images strongly depends on the SNR of these polarization images [9]. Similarly, the accuracy of the underwater geolocalization is strongly affected by noise in the *AoP* images, among other factors [19]. Thus, for these examples, and many other potential applications of polarization imaging, it is important to understand what factors influence the noise properties of both *AoP* and *DoLP*.

In this paper, we aimed to elucidate the noise and SNR properties of *AoP* and *DoLP* images captured by a single-chip polarization camera by 1) developing a rigorous theoretical model for both noise and SNR of the reconstructed polarization images; 2) utilizing Monte Carlo simulations to evaluate the SNR properties of *AoP* and *DoLP* images; and 3) performing experimental measurements to validate the theoretical models for the SNR of the polarization images.

2. Theoretical model for SNR in polarization images

2.1. Modeling input referred noise in division of focal plane polarimeters

Single-chip polarization imaging sensors combine four distinct pixelated polarization filters, repeated across the entire imaging array. The four pixelated polarization filters comprise one super-pixel and have transmission axes at 0°, 45°, 90° and 135°. The incident light on the imaging sensor is first filtered by the four individual polarization filters before being absorbed by the underlaying silicon photodiode. The photon-generated electron-hole pairs in the four photodiodes within the super-pixel configuration, which are also commonly referred to as photo-charges, will be denoted as I_0, I_{45}, I_{90} and I_{135}.

The units of I_0, I_{45}, I_{90} and I_{135} are number of electrons [e^-] accumulated at the photodiode during one exposure cycle. These photodiode charges are first converted to photovoltage, followed by voltage amplification and, finally, analog to digital conversion before transmitting the data off-chip. This is a linear conversion process characterized by a conversion gain factor, which is sensor specific and has units of digital value per electron [DV/e^-]. Hence, the digital values obtained at the output of the image sensor can be referred back to the input (i.e., photo charges at the photodiode) by dividing the output by the conversion gain. Since we are interested in the noise characteristics of the polarization images, all observations will be input referred at

OSA CONTINUUM

the photodiode node to avoid effects introduced by amplifications circuits. Hence, the *AoP* and *DoLP* values in this model are computed at the photodiode node.

The *AoP* and *DoLP* values can be computed as shown by Eqs. (1) and (2):

$$AoP = \frac{1}{2} arctan(\frac{S_2}{S_1}) \tag{1}$$

$$DoLP = \frac{\sqrt{S_1^2 + S_2^2}}{S_0}. \tag{2}$$

In the above equations, S_0, S_1 and S_2 are the first three Stokes parameters, which are computed via equations (3) through (5):

$$S_0 = I_0 + I_{90} = I_{45} + I_{135} \tag{3}$$

$$S_1 = I_0 - I_{90} \tag{4}$$

$$S_2 = I_{45} - I_{135}. \tag{5}$$

The two polarization quantities of interest, *AoP* and *DoLP*, will have uncertainty due to the noise associated with the four individual photodiodes. There are several independent noise sources in the signal path: 1) thermal noise due to the read-out electronics, such as source follower amplifier, current biasing circuitry, amplifiers, analog to digital converter and others; 2) reset noise due to the pixel transistor used to reset the photodiode and 3) shot noise associated with the photon generated electron-hole pairs in the photodiode. Reset noise is mitigated with the use of correlated double sampling circuitry, while read-out noise is minimized to few input referred electrons using advance pixel and read-out circuitry.

The photon generated electron-hole pairs will either diffuse or drift to the positive or negative end of the photodiode and contribute to the overall photocurrent. The uncertainty associated with the photon generated electron-hole pairs is described by Poisson statistics: the variance of the photon generated electron-hole pairs is equal to the mean of the electron-hole pairs in the photodiode. When large number of electron-hole pairs are generated in a photodiode, the Poisson distribution can be approximated as a normal distribution. Therefore, the noise associated with the four individual photodiodes, which is also known as shot noise, can be represented via the standard deviations of the photon generated electron-hole pairs, as shown below:

$$\sigma_{Shot\ Noise\ at\ I_{0,45,90,135}} = \sqrt{I_{0,45,90,135}}. \tag{6}$$

In addition to the shot noise, each pixel will also experience uncertainty due to the read-out noise. If the input-referred read-out noise per pixel is equal to R electrons, then the total input-referred noise per individual pixel can we represented as:

$$\sigma_{I_{0,45,90,135}} = \sqrt{\sigma^2_{Shot\ Noise\ at\ I_{0,45,90,135}} + R^2}. \tag{7}$$

It can be observed from Eq. (7), that at low light intensities, the contributions of both read-out electronics and photon shot noise are important. However, for moderate to high light intensities, the photon shot noise dominates the total noise from the pixel and the read-out noise can be ignored.

Since the noise in the *AoP* and *DoLP* quantities depend on the total noise generated by the four photodiodes within a super-pixel, standard error propagation technique can be used to determine the overall noise as shown by Eqs. (8) and (9):

$$\sigma_{AoP} = \sqrt{(\frac{\partial AoP}{\partial I_0})^2 \sigma^2_{I_0} + (\frac{\partial AoP}{\partial I_{45}})^2 \sigma^2_{I_{45}} + (\frac{\partial AoP}{\partial I_{90}})^2 \sigma^2_{I_{90}} + (\frac{\partial AoP}{\partial I_{135}})^2 \sigma^2_{I_{135}}} \tag{8}$$

OSA CONTINUUM

$$\sigma_{DoLP} = \sqrt{\left(\frac{\partial DoLP}{\partial I_0}\right)^2 \sigma_{I_0}^2 + \left(\frac{\partial DoLP}{\partial I_{45}}\right)^2 \sigma_{I_{45}}^2 + \left(\frac{\partial DoLP}{\partial I_{90}}\right)^2 \sigma_{I_{90}}^2 + \left(\frac{\partial DoLP}{\partial I_{135}}\right)^2 \sigma_{I_{135}}^2}. \quad (9)$$

From Eqs. (8) and (9), we can observe that the noise in the *AoP* and *DoLP* parameters is a weighted average of the noise from the four individual photodiodes scaled by the partial derivative of the *AoP* and *DoLP* with respect to individual photodiode charges. The partial derivatives of *AoP* and *DoLP* with respect to the individual photodiode charges are shown in the Appendix.

2.2. Modeling noise in angle and degree of linear polarization images for low light intensities

For low light intensities, both input referred read-out noise and shot noise are important factors for the total noise per pixel. After substituting the results of the partial derivatives in Eqs. (8) and (9) and further simplifying the mathematical expressions, the noise in the *AoP* and *DoLP* can be represented by Eqs. (10) and (11), respectively:

$$\sigma_{AoP} = \sqrt{\frac{1}{4 * DoLP^2 * S_0} + \frac{R^2}{2 * DoLP^2 * S_0^2}} \quad (10)$$

$$\sigma_{DoLP} = \sqrt{\frac{1 - DoLP^2 \cos(4 * AoP)}{S_0} + \frac{2R^2 * (DoLP^2 + 1)}{S_0^2}}. \quad (11)$$

In Eqs. (10) and (11), the first term is the contribution due to shot noise and the second term is the contribution of the read-out noise to the final noise figures. It can be observed that the read-out noise component in Eqs. (10) and (11) is inversely proportional to the square of the total intensity. As the light intensity increases, the contributions of the read-out noise diminish and shot noise dominates the total noise figure in angle and degree of linear polarization.

2.3. Modeling noise in angle and degree of linear polarization images for moderate light intensities

When using polarization sensors to image moderate to bright light intensities, read-out noise contributions are typically minimal compared to shot noise and can be ignored in this model. If we ignore the read-out noise in Eq. (7) and then substitute the results of the partial derivatives in Eqs. (8) and (9), the noise in the *AoP* and *DoLP* can be represented by Eqs. (12) and (13):

$$\sigma_{AoP} = \frac{1}{2 * DoLP * \sqrt{S_0}} \quad (12)$$

$$\sigma_{DoLP} = \sqrt{\frac{S_0^2 - S_1^2 + S_2^2}{S_0^3}} = \sqrt{\frac{1 - DoLP^2 \cos(4 * AoP)}{S_0}}. \quad (13)$$

These results imply that the noise in *AoP* is only affected by the incident intensity and degree of linear polarization but is independent with respect to the incident angle of polarization. However, the noise in *DoLP* is a function of all three Stokes parameters, thus indicating that *DoLP* depends on the incident intensity, angle and degree of linear polarization.

Finally, the SNR for *AoP* and *DoLP* are shown in Eqs. (14) and (15):

$$SNR_{AoP} = \frac{\pi}{\sigma_{AoP}} = 2\pi * DoLP * \sqrt{S_0} \quad (14)$$

OSA CONTINUUM

$$SNR_{DoLP} = \frac{DoLP}{\sigma_{DoLP}} = \sqrt{\frac{(S_1^2 + S_2^2)S_0}{S_0^2 - S_1^2 + S_2^2}} = \sqrt{\frac{DoLP^2 * S_0}{1 - DoLP^2 * \cos(4 * AoP)}}. \quad (15)$$

In Eq. (14), the maximum possible *AoP* is used in the numerator (i.e. π radians) to avoid penalizing low incident angles of polarization (e.g., $AoP = 0°$). From the above equations, we can observe that the SNR of *AoP* depends on both light intensity and *DoLP*, while the SNR of *DoLP* depends on the first three Stokes parameters (contained within the definition of *DoLP*) in a more complex manner.

2.4. Output referred SNR for angle and degree of linear polarization

Up to this point, we have derived a closed-form solution for SNR for the angle and degree of linear polarization values referred at the input node (i.e., at the photodiode node). However, when we use polarization imaging sensors, we obtain pixel data that has been converted from the photodiode charges to an output digital value, which is a linear conversion process characterized by the sensor's conversion gain factor. For example, the digital output value for the four pixels can be represented by Eq. (16):

$$DV_{0,45,90,135} = K * I_{0,45,90,135}. \quad (16)$$

In Eq. (16), DV_x represents the digital value from one of the four pixels within the super-pixel configuration and K is the conversion gain in unit digital value per electron [DV/e$^-$]. The *AoP* and *DoLP* information at the output can be computed using Eqs. (1) and (2) by substituting the photodiode charges (I_x) with the output digital value (DV_x). Since *AoP* and *DoLP* are unitless quantities, (i.e., the conversion gain in the numerator is canceled by the conversion gain in the denominator, provided that all pixels have the same conversion gain), the input referred and output referred *AoP* and *DoLP* values are the same.

However, the output referred *AoP* and *DoLP* noise is $\sqrt{K}$ times smaller than the input referred *AoP* and *DoLP* noise, respectively, as shown by Eqs. (17) and (18):

$$\sigma_{AoP@output} = \frac{1}{2}\frac{1}{DoLP}\frac{1}{\sqrt{K * S_0}} = \frac{\sigma_{AoP@input}}{\sqrt{K}} \quad (17)$$

$$\sigma_{DoLP@output} = \sqrt{\frac{K^2 * (S_0^2 - S_1^2 + S_2^2)}{K^3 * S_0^3}} = \frac{\sigma_{DoLP@input}}{\sqrt{K}}. \quad (18)$$

Substituting Eqs. (17) and (18) into Eqs. (14) and (15), we can observe that the output referred SNR is $\sqrt{K}$ times higher than the input referred SNR for both *AoP* and *DoLP* parameters. Since *AoP* and *DoLP* information is typically computed at the output, the SNR of *AoP* and *DoLP* images can be improved by increasing the gain of the amplification circuitry at the cost of decreasing the imager dynamic range by the same amount. To avoid confusion when comparing SNRs between different polarization images, where the signal gain might not be the same, it is customary to talk about input referred noise and input referred SNR of the polarization images.

2.5. Simulating input referred SNR for angle and degree of linear polarization

Figure 1 shows the simulated SNR for *AoP* and *DoLP* as a function of various incident light intensities and *DoLP* levels using Eqs. (14) and (15). The incident light intensity is represented as a number of incident photons per photodiode for one exposure period. We also assumed that the quantum efficiency for the sensor was 100% (i.e., each incident photon generates one electron-hole pair on the photodiode). Since most division-of-focal-plane sensors have pixel well

OSA CONTINUUM

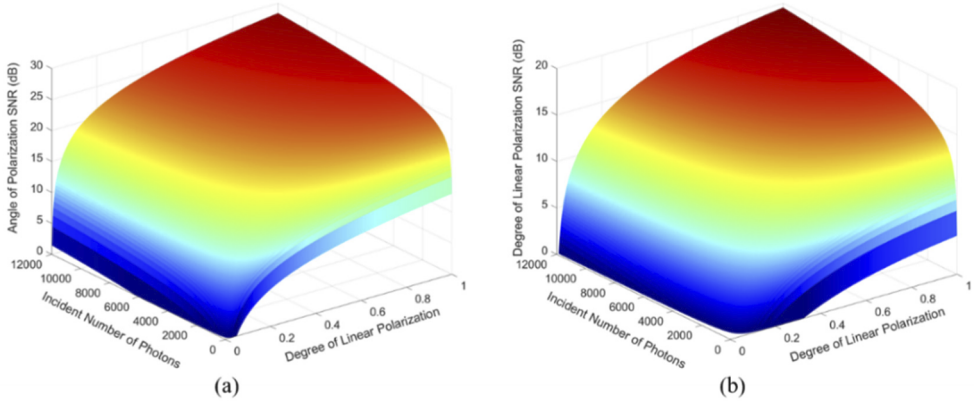

Fig. 1. Simulated SNR of (a) AoP and (b) DoLP as a function of light intensity and DoLP. The simulation results are obtained using closed form solution for the SNR of AoP and DoLP, respectively.

depths of ~10,000e$^-$ [1,3], the range for the incident light intensity was selected to be between 10 and 10,000 photons per photodiode per exposure period.

The SNR of *AoP* was observed to increase with higher incident intensity and higher *DoLP*. The SNR of the *DoLP* also followed a similar trend but had smaller overall SNR compared to the *AoP* SNR. To summarize, linearly polarized light produced the highest SNR in both *AoP* and *DoLP* images. Furthermore, increased light intensity also yielded higher SNR in polarization images.

3. Monte Carlo simulation of the AoP and DoLP SNR

In the previous section, we used an error propagation technique to derive a closed-form solution for the SNR for *AoP* and *DoLP* quantities. Next, we used a Monte Carlo (MC) approach to validate the accuracy of the simulation results obtained from the theoretical model described by Eqs. (13) and (14). MC simulations use random sampling of the input variables together with a noise-less mathematical model to compute statistics at the output. The statistics of the input variable are known *a priori*, which enables proper sampling of the input signal before computing the final output. After many individual simulations are performed, the statistics at the output can be computed. This process is very attractive because each run is independent and, with the utilization of graphics processors, statistics at the output signal can be quickly computed without the need of deriving complicated error propagation equations [30].

For the MC simulations, we used equations (1) through (6) to determine the SNR for *AoP* and *DoLP* quantities. Equations (1) through (5) established the mathematical framework for computing *AoP* and *DoLP* quantities based on four noise-less input variables (i.e., accumulated photo charges in the four photodiodes under the pixelated polarization filters). Equation (6) provided statistics for the four input variables, which were used to guide the random draw of values for the four photodiodes for a given mean signal and compute the two polarization quantities of interest.

Instead of specifying a range of photo charges accumulated on the four individual photodiodes in the MC simulation, we specified three different input variables: intensity, angle and degree of linear polarization for the incident light. Based on these three inputs, we computed the standard deviations on the reconstructed angle and degree of linear polarization. For a given light intensity, angle and degree of linear polarization, the photon generated electron-hole pairs at a photodiode were computed using Eq. (16), under the assumption that each incident photon generates one

OSA CONTINUUM

electron-hole pair in the photodiode:

$$I(\theta) = \frac{1}{2} I_0[1 + DoLP * \cos(2\theta - 2 * AoP)]. \tag{19}$$

In Eq. (16), I_0 is the total number of incident photons per pixelated filter during one exposure period and Θ is the transmission axis of the individual pixelated polarization filter. After the mean photo charges in the four individual photodiodes were computed using Eq. (16), the standard deviation within each photodiode was defined by the shot noise represented by Eq. (6). Hence, for the MC simulation, we acquired 20,000 samples per photodiode from a Poisson distribution with a mean signal defined by Eq. (16). For each randomly selected sample, *AoP* and *DoLP* quantities were computed using equations (1) through (5). The noise for the *AoP* and *DoLP* quantities were computed as the standard deviation of the resulting *AoP* and *DoLP* quantities from all 20,000 input samples. The SNR was accordingly computed by dividing the mean with the standard deviation of the output polarization signal.

The SNR for *AoP* and *DoLP* quantities computed via a MC simulation are shown in Fig. 2. In these simulation results, the incident *AoP* was set to 60°, while the *DoLP* was varied between 0 and 1. The root mean square error between the theoretical and MC results for AoP and DoLP were 0.59 and 0.60, respectively. These results demonstrate that our theoretical model and MC simulation matched very well. The RMSE could be further decreased by increasing the number of randomly selected input samples at the expense of longer simulation time. The MC approach demonstrates the feasibility of providing quick estimate for the SNR of *AoP* and *DoLP* without deriving complicated mathematical framework.

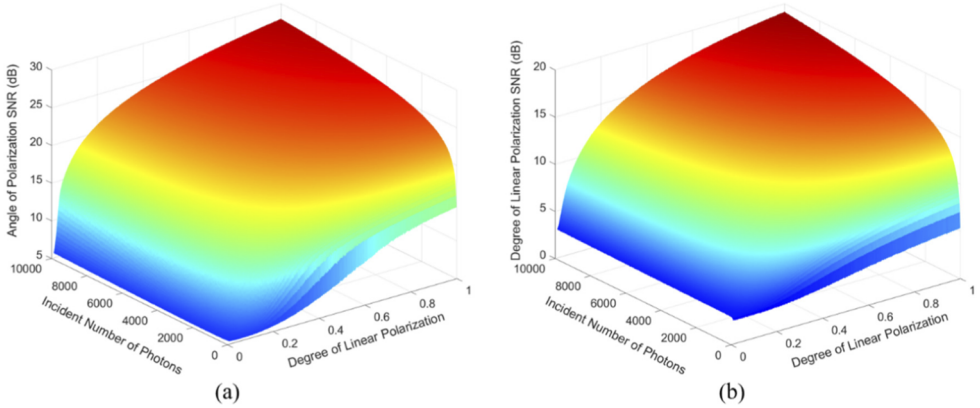

Fig. 2. (a) Monte Carlo simulation of AoP SNR as a function of light intensity and DoLP and (b) Monte Carlo simulation of DoLP SNR as a function of light intensity and DoLP.

4. Experimental data and results

4.1. Experiment setup

The next step was to measure the SNR of the reconstructed *AoP* and *DoLP* quantities using a commercially available polarization sensor and compare these results to our theoretical model. To this end, a narrow-band red LED (LZ4-00R108, OSRAM) was coupled to an input port of an integrating sphere to create uniform and depolarized output illumination. The output from the integrating sphere passed through a linear polarizer (LPVISB100-MP, Thorlabs) followed by a quarter-wave plate (WPMQ10M-633, Thorlabs) before illuminating a polarization sensor (FLIR Blackfly S BFS-U3-51S5P).

OSA CONTINUUM

The linear polarization filter and quarter wave plate were mounted on separate computer-controlled rotational stages and independently rotated between 0° to 180° in increments of 6°. The independent rotation of these two polarization elements, helped generate a variety of different angles and degree of linear polarization for the incident illumination on the image sensor.

The image sensor was equipped with a 50mm Tamron F/2.8 lens (M112FM50). The aperture of the lens was set to f/16 to minimize optical crosstalk between neighboring photodiodes. The exposure time of the polarization sensor was swept between 200 µs to 47 ms in steps of either 1 ms or 2 ms. A total of 1,000 images were collected for each incident illumination (19 different exposures) and different *DoLP* level. Four pixels in the middle of the image sensor were selected for analysis. If one of the four pixels was saturated or clamped to the lowest output value, these pixels were not used to compute polarization information. The data from the four pixels were referred back to the input by dividing the digital numbers by the conversion gain. Next, input referred angle and degree of linear polarization were computed. Mean and standard deviation were computed on the input referred data from the 1,000 images.

4.2. Computing conversion gain

The conversion gain for the image sensor was computed using photon transfer curve (PTC) method published in the literature and shown in Fig. 3 [31]. Briefly, 10 sets of 1,000 images were collected as exposure was varied between 20 µs and 50 msec. Dark frames (n=1,000) were collected with no light input to the camera and averaged to create an offset image. Figure 3 shows the variance vs. average signal minus the offset. The conversion gain of the sensor was equal to the slope of this curve (i.e., 0.35 DV/e^-).

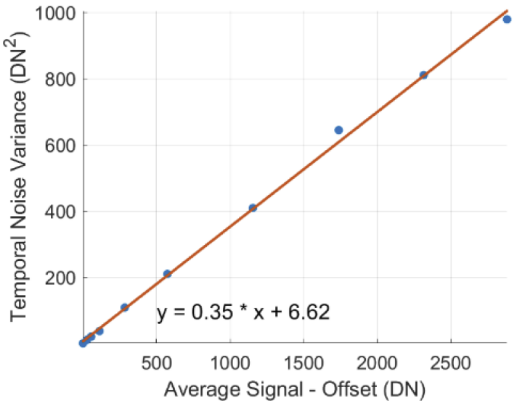

Fig. 3. Photon Transfer Curve: noise variance versus average effective output signal

4.3. Experiment results and discussion

Figure 4 shows the SNR for *AoP* and *DoLP* computed from the data collected from a division of focal plane polarimeter, along with the theoretical SNR for *AoP* and *DoLP* (i.e., closed form solutions). The measured SNR for both *AoP* and *DoLP* closely followed the theoretical model.

Figure 5 shows 2-D cross-sectional profiles from the data presented in Fig. 4 for SNR of the *AoP* (Fig. 5-(a)) and *DoLP* (Fig. 5-(b)) for three different light intensities. In these plots, it can be observed that higher *SNR* was achieved at larger incident intensities and higher *DoLP* for the incident light. The figure also shows the results of the theoretical models when the read-out noise is either included or not. For low light intensities (204 incident photons), the experimental data matched better with the theoretical model that included the read-out noise because both read-out noise and shot noise are important contributors to the total noise per pixel in low light

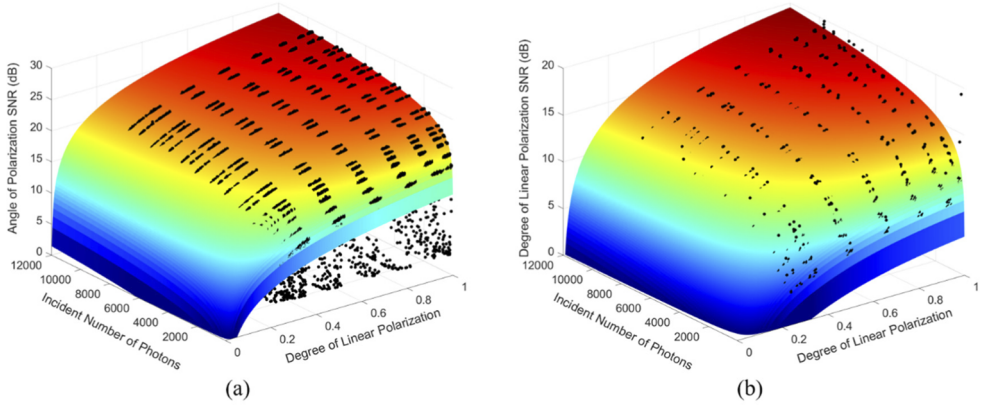

Fig. 4. (a) Experimental and theoretical SNR of AoP and (b) experimental and theoretical SNR of DoLP

settings. However, as the incident intensity was increased to ~2,000 photons or higher, both theoretical models converged to the same result and matched the experimental data very well. In these cases, the shot noise dominates the total noise figure and contributions of the read-out noise are minimal. Due to noise in the optical setup, several data points deviated from the theoretical model especially at low light exposure time.

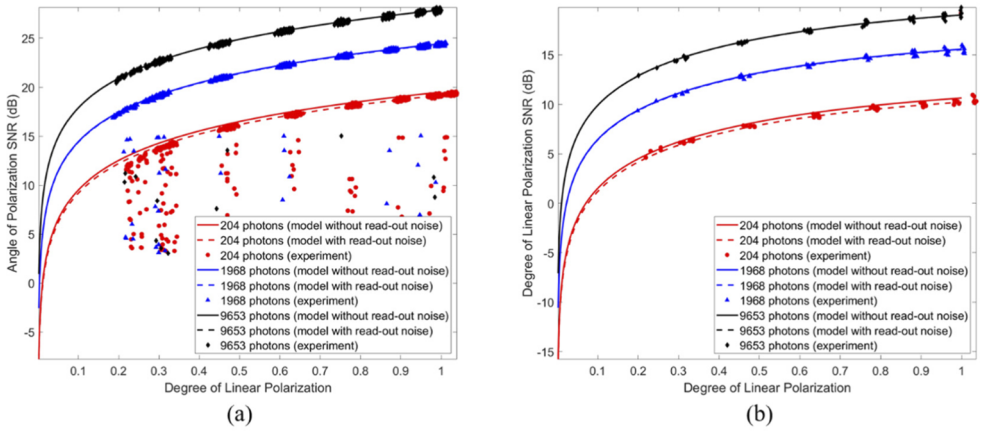

Fig. 5. (a) 2-D cross profile of experimental and theoretical SNR of AoP and (b) 2-D cross profile of experimental and theoretical SNR of DoLP

Figure 6 shows SNR for *AoP* for different incident angle of polarization and *DoLP* levels. It is interesting to note that the SNR of *AoP* quantity is independent on the incident angle of polarization as predicted by the theoretical results. Higher SNR of *AoP* quantity is achieved with larger incident intensity (Fig. 6(a)) and highly polarized light (i.e., higher *DoLP* of the incident light; Fig. 6(b)). For low light intensities (~200 incident photons), the inclusion of the read-out noise in the theoretical model better represented the experimental data.

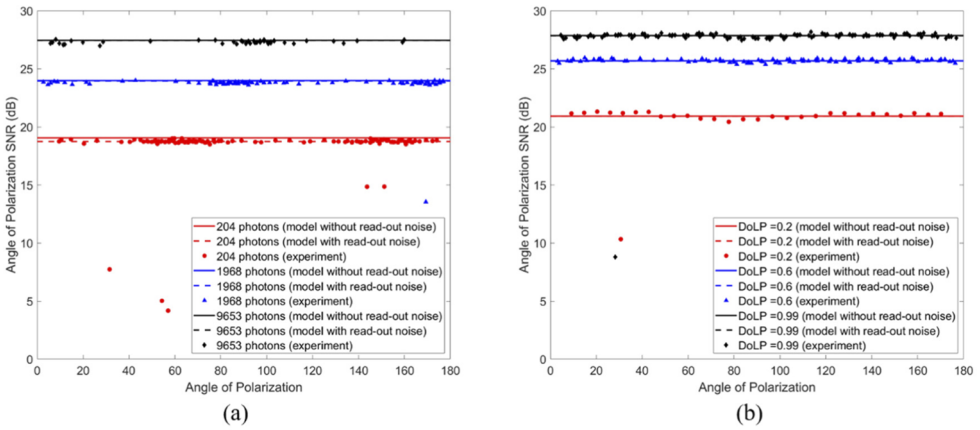

Fig. 6. 2-D cross profile of experimental and theoretical SNR of *AoP* as a function of different incident angles of polarization for (a) different light intensities and (b) different degrees of linear polarization

5. Conclusion

In this paper, we presented both theoretical and experimental data for *SNR* in *AoP* and *DoLP* quantities. The emergence of commercial polarization imaging sensors has reinvigorated the field of polarization imaging. Many novel applications have emerged in the last couple of years, ranging from discoveries in the biomedical field to remote sensing. As these and other new applications emerge, it is important to understand the various contributions of noise in the reconstructed polarization images. Optimization of imaging setups is necessary to acquire better polarization data. In this spirit, we derived a theoretical model for the expected noise and SNR in polarization images. Experimental data was collected from a commercially available polarization sensors and these data matched closely with the theoretical model.

From our theoretical model, we can state that the SNR for *AoP* data depends on both intensity and degree of linear polarization. The SNR for *DoLP* data depends on all three quantities of the incident light: intensity, angle and degree of linear polarization. Furthermore, the output referred *AoP* and *DoLP* noise was $\sqrt{K}$ times smaller compare to the input referred *AoP* and *DoLP* noise (where K is the conversion gain of the sensor). Increasing the amplification would decrease the dynamic range of the sensor and has to be carefully optimized for a given application. The Monte Carlo approach has been extensively used to estimate noise in both linear and non-linear systems. The simplicity of this method can help guide the development and optimization of division of focal plane sensors that utilize an alternative super-pixel configuration. These guidelines can help optimize future polarization-based imaging applications, such as underwater based geolocalization, microstructural organization in biological tissues, early cancer detection and others.

Appendix: Partial derivatives of angle and degree of linear polarization

The final result of the partial derivative of the angle of polarization and degree of linear polarization with respect to the photo charges at the four different photodiodes are shown by equations (A1) through (A8):

$$\frac{\partial AoP}{\partial I_0} = -\frac{1}{2} * \frac{I_{45} - I_{135}}{(I_0 - I_{90})^2 + (I_{45} - I_{135})^2} = -\frac{1}{2} * \frac{S_2}{S_1^2 + S_2^2} \tag{A1}$$

OSA CONTINUUM

$$\frac{\partial AoP}{\partial I_{45}} = \frac{1}{2} * \frac{I_0 - I_{90}}{(I_0 - I_{90})^2 + (I_{45} - I_{135})^2} = \frac{1}{2} * \frac{S_1}{S_1^2 + S_2^2} \tag{A2}$$

$$\frac{\partial AoP}{\partial I_{90}} = \frac{1}{2} * \frac{I_{45} - I_{135}}{(I_0 - I_{90})^2 + (I_{45} - I_{135})^2} = \frac{1}{2} * \frac{S_2}{S_1^2 + S_2^2} \tag{A3}$$

$$\frac{\partial AoP}{\partial I_{135}} = -\frac{1}{2} * \frac{I_0 - I_{90}}{(I_0 - I_{90})^2 + (I_{45} - I_{135})^2} = -\frac{1}{2} * \frac{S_1}{S_1^2 + S_2^2} \tag{A4}$$

$$\begin{aligned} \frac{\partial DoLP}{\partial I_0} &= \frac{I_0 - I_{90}}{(I_0 + I_{90})\sqrt{(I_0 - I_{90})^2 + (I_{45} - I_{135})^2}} - \frac{\sqrt{(I_0 - I_{90})^2 + (I_{45} - I_{135})^2}}{(I_0 + I_{90})^2} \\ &= \frac{S_1}{S_0\sqrt{S_1^2 + S_2^2}} - \frac{\sqrt{S_1^2 + S_2^2}}{S_0^2} \end{aligned} \tag{A5}$$

$$\frac{\partial DoLP}{\partial I_{45}} = \frac{I_{45} - I_{135}}{(I_0 + I_{90})\sqrt{(I_0 - I_{90})^2 + (I_{45} - I_{135})^2}} = \frac{S_2}{S_0\sqrt{S_1^2 + S_2^2}} \tag{A6}$$

$$\begin{aligned} \frac{\partial DoLP}{\partial I_{90}} &= -\frac{I_0 - I_{90}}{(I_0 + I_{90})\sqrt{(I_0 - I_{90})^2 + (I_{45} - I_{135})^2}} - \frac{\sqrt{(I_0 - I_{90})^2 + (I_{45} - I_{135})^2}}{(I_0 + I_{90})^2} \\ &= -\frac{S_1}{S_0\sqrt{S_1^2 + S_2^2}} - \frac{\sqrt{S_1^2 + S_2^2}}{S_0^2} \end{aligned} \tag{A7}$$

$$\frac{\partial DoLP}{\partial I_{135}} = -\frac{I_{45} - I_{135}}{(I_0 + I_{90})\sqrt{(I_0 - I_{90})^2 + (I_{45} - I_{135})^2}} = -\frac{S_2}{S_0\sqrt{S_1^2 + S_2^2}}. \tag{A8}$$

Funding. Air Force Office of Scientific Research (FA9550-18-1-0278); Office of Naval Research (N00014-19-1-2400); National Science Foundation (1761561).

Disclosures. The authors declare no conflicts of interest.

References

1. https://www.sony-semicon.co.jp/e/products/IS/polarization/product.html.
2. T. Mu, S. Pacheco, Z. Chen, C. Zhang, and R. Liang, "Snapshot linear-Stokes imaging spectropolarimeter using division-of-focal-plane polarimetry and integral field spectroscopy," Sci. Rep. **7**(1), 1–11 (2017).
3. V. Gruev, R. Perkins, and T. York, "CCD polarization imaging sensor with aluminum nanowire optical filters," Opt. Express **18**(18), 19087–19094 (2010).
4. Y. Maruyama, T. Terada, T. Yamazaki, Y. Uesaka, M. Nakamura, Y. Matoba, K. Komori, Y. Ohba, S. Arakawa, and Y. Hirasawa, "3.2-MP Back-Illuminated Polarization Image Sensor With Four-Directional Air-Gap Wire Grid and 2.5-μm Pixels," IEEE Trans. Electron Devices **65**(6), 2544–2551 (2018).
5. X. Tu, S. McEldowney, Y. Zou, M. Smith, C. Guido, N. Brock, S. Miller, L. Jiang, and S. Pau, "Division of focal plane red–green–blue full-Stokes imaging polarimeter," Appl. Opt. **59**(22), G33–G40 (2020).
6. G. Myhre, W.-L. Hsu, A. Peinado, C. LaCasse, N. Brock, R. A. Chipman, and S. Pau, "Liquid crystal polymer full-stokes division of focal plane polarimeter," Opt. Express **20**(25), 27393–27409 (2012).
7. W.-L. Hsu, G. Myhre, K. Balakrishnan, N. Brock, M. Ibn-Elhaj, and S. Pau, "Full-Stokes imaging polarimeter using an array of elliptical polarizer," Opt. Express **22**(3), 3063–3074 (2014).
8. X. Zhao, A. Bermak, F. Boussaid, and V. G. Chigrinov, "Liquid-crystal micropolarimeter array for full Stokes polarization imaging in visible spectrum," Opt. Express **18**(17), 17776–17787 (2010).
9. T. York, S. B. Powell, S. Gao, L. Kahan, T. Charanya, D. Saha, N. W. Roberts, T. W. Cronin, J. Marshall, S. Achilefu, S. P. Lake, B. Raman, and V. Gruev, "Bioinspired Polarization Imaging Sensors: From Circuits and Optics to Signal Processing Algorithms and Biomedical Applications," Proc. IEEE **102**(10), 1450–1469 (2014).
10. M. Garcia, C. Edmiston, R. Marinov, A. Vail, and V. Gruev, "Bio-inspired color-polarization imager for real-time in situ imaging," Optica **4**(10), 1263–1271 (2017).
11. M. Garcia, T. Davis, S. Blair, N. Cui, and V. Gruev, "Bioinspired polarization imager with high dynamic range," Optica **5**(10), 1240–1246 (2018).
12. M. Zhang, X. Wu, N. Cui, N. Engheta, and J. Van der Spiegel, "Bioinspired focal-plane polarization image sensor design: from application to implementation," Proc. IEEE **102**(10), 1435–1449 (2014).

OSA CONTINUUM

13. Z. Zhang, F. Dong, T. Cheng, K. Qiu, Q. Zhang, W. Chu, and X. Wu, "Nano-fabricated pixelated micropolarizer array for visible imaging polarimetry," Rev. Sci. Instrum. **85**(10), 105002 (2014).
14. S. S. Stafeev, V. V. Kotlyar, A. G. Nalimov, M. V. Kotlyar, and L. O'Faolain, "Subwavelength gratings for polarization conversion and focusing of laser light," Photonics and Nanostructures-Fundamentals and Applications **27**, 32–41 (2017).
15. H. Kim, J. Park, I. Joe, D. Kwon, J. H. Kim, D. Cho, T. Lee, C. Lee, H. Park, and S. Hong, "5.6 A 1/2.65 in 44Mpixel CMOS Image Sensor with 0.7 µm Pixels Fabricated in Advanced Full-Depth Deep-Trench Isolation Technology," in *2020 IEEE International Solid-State Circuits Conference-(ISSCC)*, (IEEE, 2020), 104–106.
16. M. Kulkarni and V. Gruev, "Integrated spectral-polarization imaging sensor with aluminum nanowire polarization filters," Opt. Express **20**(21), 22997–23012 (2012).
17. V. Narayanamurthy, P. Padmapriya, A. Noorasafrin, B. Pooja, K. Hema, K. Nithyakalyani, and F. Samsuri, "Skin cancer detection using non-invasive techniques," RSC Adv. **8**(49), 28095–28130 (2018).
18. T. Novikova, A. Pierangelo, A. De Martino, A. Benali, and P. Validire, "Polarimetric imaging for cancer diagnosis and staging," Optics and photonics news **23**(10), 26–33 (2012).
19. S. B. Powell, R. Garnett, J. Marshall, C. Rizk, and V. Gruev, "Bioinspired polarization vision enables underwater geolocalization," Sci. Adv. **4**(4), eaao6841 (2018).
20. G. Van Harten, J. De Boer, J. Rietjens, A. Di Noia, F. Snik, H. Volten, J. Smit, O. Hasekamp, J. Henzing, and C. Keller, "Atmospheric aerosol characterization with a ground-based SPEX spectropolarimetric instrument," Atmos. Meas. Tech. **7**(12), 4341–4351 (2014).
21. L. M. Eshelman, M. J. Tauc, and J. A. Shaw, "All-sky polarization imaging of cloud thermodynamic phase," Opt. Express **27**(3), 3528–3541 (2019).
22. L. Cartron, N. Josef, A. Lerner, S. D. McCusker, A.-S. Darmaillacq, L. Dickel, and N. Shashar, "Polarization vision can improve object detection in turbid waters by cuttlefish," J. Exp. Mar. Biol. Ecol. **447**, 80–85 (2013).
23. P. C. Brady, A. A. Gilerson, G. W. Kattawar, J. M. Sullivan, M. S. Twardowski, H. M. Dierssen, M. Gao, K. Travis, R. I. Etheredge, A. Tonizzo, A. Ibrahim, C. Carrizo, Y. Gu, B. J. Russell, K. Mislinski, S. Zhao, and M. E. Cummings, "Open-ocean fish reveal an omnidirectional solution to camouflage in polarized environments," Science **350**(6263), 965–969 (2015).
24. G. M. Calabrese, P. C. Brady, V. Gruev, and M. E. Cummings, "Polarization signaling in swordtails alters female mate preference," Proc. Natl. Acad. Sci. **111**(37), 13397–13402 (2014).
25. D. Miyazaki and S. Hashimoto, "Uncalibrated photometric stereo refined by polarization angle," Optical Review, 1–15 (2021).
26. L. Yang, F. Tan, A. Li, Z. Cui, Y. Furukawa, and P. Tan, "Polarimetric dense monocular slam," in *Proceedings of the IEEE conference on computer vision and pattern recognition*, 2018), 3857–3866.
27. D. Zhu and W. A. Smith, "Depth from a polarisation+ rgb stereo pair," in *Proceedings of the IEEE/CVF Conference on Computer Vision and Pattern Recognition*, 2019), 7586–7595.
28. R. M. Patel, R. M. Castile, M. J. Jenkins, S. P. Lake, and R. H. Brophy, "Microstructural and Mechanical Properties of the Anterolateral Ligament of the Knee," The American Journal of Sports Medicine **49**(1), 172–182 (2021).
29. M. V. Smith, R. M. Castile, R. H. Brophy, A. Dewan, D. Bernholt, and S. P. Lake, "Mechanical properties and microstructural collagen alignment of the ulnar collateral ligament during dynamic loading," The American journal of sports medicine **47**(1), 151–157 (2019).
30. D. Ramon, F. Steinmetz, D. Jolivet, M. Compiègne, and R. Frouin, "Modeling polarized radiative transfer in the ocean-atmosphere system with the GPU-accelerated SMART-G Monte Carlo code," Journal of Quantitative Spectroscopy and Radiative Transfer **222-223**, 89–107 (2019).
31. J. R. Janesick, *Photon transfer DN→ λ* (SPIE, Bellingham, Wash, 2007).